Aerospace Science and Technology 13 (2009) 267–276

Contents lists available at ScienceDirect

Aerospace Science and Technology

www.elsevier.com/locate/aescte

Numerical and experimental study of flow field characteristics of an iced airfoil

Masoud Mirzaei [a,*,1], Mohammad A. Ardekani [b,2], Mehdi Doosttalab [c,3]

[a] Department of Aerospace, K.N. Toosi University of Technology, 322 Mirdamad Ave. West, 19697, Tehran, Iran
[b] Iranian Organization of Science and Technology, No. 71, Forsat St, Ferdousi Sq, Tehran, Iran
[c] Department of Aerospace, K.N. Toosi University of Technology, Iran

ARTICLE INFO

Article history:
Received 6 November 2007
Received in revised form 3 May 2009
Accepted 13 May 2009
Available online 19 May 2009

Keywords:
Iced-airfoil
Numerical and wind tunnel experiments
Unsteady flow
Hot-wire

ABSTRACT

In this paper, characteristics of separated bubbles and unsteady features of flow fields around a glaze-iced airfoil are investigated. The research was performed using both experimental and numerical approaches. The airfoil was a natural laminar airfoil (NLF-0414) and the ice is considered as the glaze accretion. The experimental measurements were carried out using hot-wire anemometry at Reynolds number of 0.5×10^6 and angle of attack ranging from 0° to 6°. In numerical calculations, N–S equations were adopted as governing equations and finite-volume technique was employed to solve the equations. Numerical calculations were performed at Reynolds numbers of 0.5×10^6 and 1.8×10^6. CFD results and experimental data indicated increasing in the bubble length with increasing in airfoil angle-of-attack. The results showed two separated bubbles in different sizes and also unsteadiness behavior of the flow field which led to low frequency oscillation in lift coefficient with the order of 10 Hz. The frequency of the vortex structures observed in the shear layer measured with hot-wire and it is found that the frequency was in the range of 100 Hz. This frequency was reduced with increasing the angle-of-attack. Vortex shedding was also observed at the downstream of the reattachment location.

1. Introduction

Ice accretion on the leading edge of an aircraft wings changes the shape of the wings surface and consequently changes the flow field. This phenomenon influences the pressure distribution and aerodynamic characteristics of the wings and causes increment in drag, reduction in maximum lift, premature stall, and vibration of the wings and finally losing the control of the aircraft. Since degradation of these aerodynamic parameters plays a vital role in flight safety, understanding the flow field and prediction of these penalties are very important.

Glaze is a wet growth ice formed at a temperature around 0 °C and high liquid water content. It occurs when only a fraction of the water droplets freezes upon impact while the remainder droplets run back along the surface or along and freeze downstream. Glaze-ice grows in both upper and lower surfaces of the wing, near leading edge and has backward step geometry. Glaze-ice accretion dangerously affects and alters the shape of the original wing surface producing aerodynamic penalties much more severe than rime ice accretion can cause. Schematic of the flow field on the upper surface of a NLF-0414 airfoil with leading edge glaze-ice accretion is presented in Fig. 1(a). This flow field is quite different from that of the clean airfoil and this leads to degradation of the aerodynamic performance of a wing. Fig. 1(b) represents lift coefficient-angle of attack curves of a clean and an iced NLF-0414 airfoil. It can be seen that the ice accretion has caused premature stall and reduction in slope of the lift curve.

Bragg [2] described that, the flow separates off the edge of the glaze ice due to strong adverse pressure gradient and a bubble forms aft of the ice accretion. A shear layer forms between this region and the inviscid flow above the bubble. Vortex motion in the shear layer improves mixing between the separated bubble and the inviscid flow. This phenomenon strengthens the pressure recovery and allows the flow to reattach to the airfoil surface downstream of the separation bubble at low angles-of-attack. At higher angles-of-attack the pressure recovery may not be achieved and stall may occur. The shape and size of the separation bubbles and reattachment point vary with time due to the flow unsteadiness. Moreover vortex shedding may happen along the downstream of the reattachment point. Gurbacki and Bragg [6,7] performed some investigations on unsteady surface–pressure distribution for NACA 0012 airfoil with leading-edge, glaze-ice accretions. They used oil-flow visualization technique, and Particle Image Velocimetry (PIV). They showed that the mean reattachment length increases as the

* Corresponding author. Tel.: +98 21 77791044; fax: +98 21 77791045.
E-mail address: mirzaei@kntu.ac.ir (M. Mirzaei).
[1] Associate professor.
[2] Assistant professor.
[3] Graduate student.

1270-9638/$ – see front matter
doi:10.1016/j.ast.2009.05.002

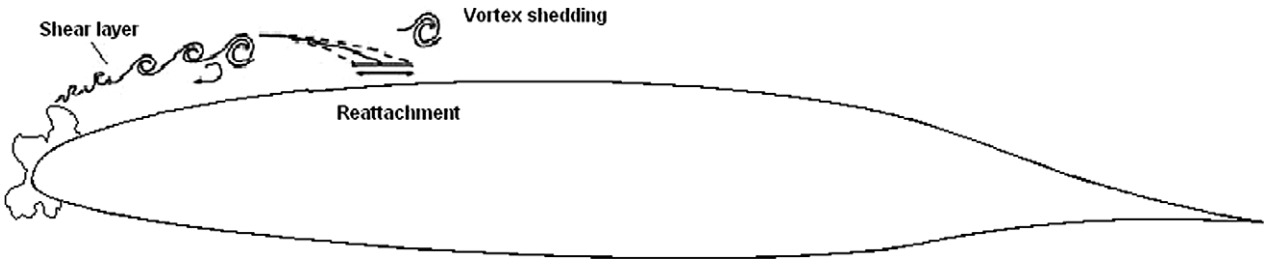

(a)

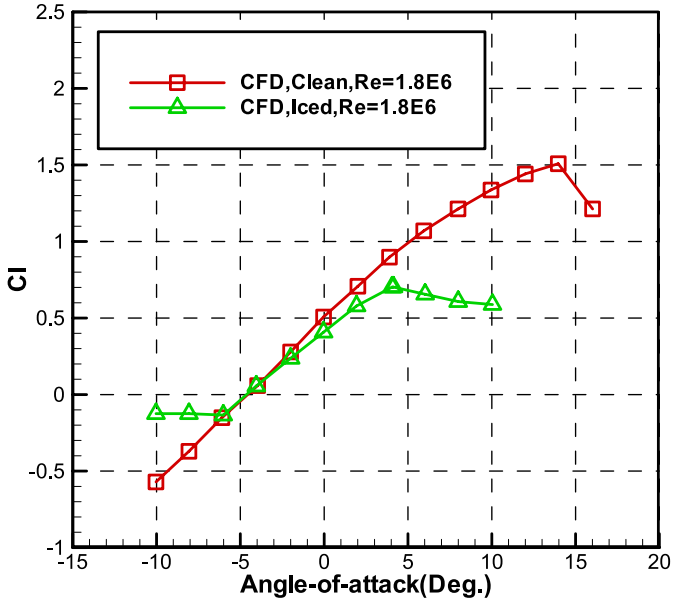

(b)

Fig. 1. (a) Schematic of separation bubble on the upper surface of a NLF-0414 airfoil with leading edge glaze-ice accretion. (b) Lift coefficient – angle of attack curves of a clean NLF-0414 airfoil and NLF-0414 airfoil with leading edge glaze-ice accretion.

angles-of-attack is increased and stall occurred at about an angle-of-attack that is 10° less than that of clean airfoil. Power spectra of time-dependent surface-pressure data at mean reattachment location presented non-dimensional frequency or Strouhal number ranging from $St = 0.53$ to 0.73. These frequencies corresponded to the shear-layer vortices. Moreover, the low-frequency unsteadiness of lift coefficient was reported near stall with $St = 0.01$. This low frequency often associated with vertical flapping motion of the separated shear layer. Kiya and Sasaki [12] and also Cherry et al. [3] observed vortex shedding over blunted flat plate geometries at regular, or dominant, frequencies. Both investigations identified a vertical flapping motion of the separated shear layer near the separation line that accompanied fluctuating bubble reattachment.

Jacobs and Bragg [10] performed an investigation on NACA0012 airfoil with two and three dimensional simulated leading edge, glaze-ice accretion using surface oil-flow visualization and Particle Image Velocimetry (PIV). Time-averaged PIV results showed a primary recirculation with clockwise rotation defined by a shear layer and a smaller, counter-clockwise secondary recirculation aft of the ice accretion; both recirculation regions were similar to backward-facing step flow field. Vortices were detected at the shear layer and downstream of the reattachment location. Two local maximum RMS velocities were also detected at the shear layer, aft of the ice accretion.

In the present work, for the first time the frequency of the separated bubbles and shear layer has been investigated using hot-wire anemometry on a NLF-0414 airfoil and the results are compared qualitatively with those of similar works were performed using PIV. Moreover the problem was simulated using CFD calculations and the results are compared with experimental data.

2. Experimental methods

All the experiments were carried out in the low speed wind tunnel of Iranian Research Organization of Science and Technology (IROST) center. The wind tunnel is a closed-return wind-tunnel that is principally used for two-dimensional testing. It can operate at 0 to 30 m/s. A heat exchanger, honeycomb and three turbulence reduction screens are located at the inlet settling chamber. The test section dimensions are 60-centimeter wide, 60-centimeter high, 200-centimeter long and the contraction ratio between the settling chamber and test section is 7.5:1 and the free stream turbulence intensity level is about 0.1%. Desired airspeed is achieved using a variable frequency drive, which controls a 15-Kw motor. Fig. 2 shows a picture of the wind tunnel facilities.

The airfoil model used for this investigation was NLF-0414 with 40-centimeter in chord, 60-centimeter in span, and was mounted vertically in the test section. The simulated Ice-shape was based on a leading edge glaze-ice accretion investigated in the IRT Glenn research center wind tunnel with the geometry shown in Fig. 3. It was acquired during a 22.5-minute spray time at −5.5 °C and −1.1 °C with a liquid water content and a median volumetric diameter of 0.54 g/m^3 and 20 μm respectively at −1.7° angle-of-attack. More details about the ice shape may be found in [1]. A two-dimensional high precision geometrically-scaled Plexiglas glaze-ice shape cut by LASER is attached to the leading edge of the model.

The flow field measurements require some equipment both inside and outside of the test section including: A traversing mechanism mounted on the top wall of the test-section shown in Fig. 4. a step-motor to control the vertical and horizontal position of the

Fig. 2. Wind tunnel setup.

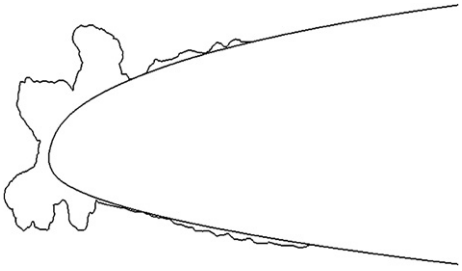

Fig. 3. Simulated leading edge glaze-ice accretion.

measurement probe of the hot-wire system with the accuracy of ± 0.1 mm, and a computer program to manage the positioning system. The spanwise location of the measurement plane was fixed at 50% of span (30 Cm). A FSS, Inc. Model WUTTLL hot-wire probe was used in all measurements. This arrangement measures the magnitude of the streamwise velocity component. The hot-wire sensor was positioned between 0.5 mm and 0.7 mm above the airfoil surface. This offset distance was regularly checked and its effects are accounted in velocity profile data. In general, the profile measurements were acquired close enough to capture the reattachment location with accuracy of 2.5% of chord. The spacing of the sampling points in the vertical direction was adjusted based on the thickness of the separation bubble or boundary layer. The profiles consisted of 30 points with non-uniform distribution from the airfoil surface to the free stream. These velocity profile data were acquired at $\alpha = 0^\circ, 2^\circ, 4^\circ$ and 6° and Reynolds number of 0.5×10^6. The calibration of the sensor was performed at the wind tunnel test section. This calibration has been carried out several times during the tests to ensure that there was no drift due to sensor contamination or other effects. For each point, data were acquired at a rate of 5000 samples per second for ten seconds interval. The voltages were temperature corrected (to account in temperature variation during the tests). The mean streamwise velocity (u), Root-Mean Square (RMS) of the velocity fluctuations (u_{rms}) and vortex frequency data were calculated from the time series data.

The uncertainty of the hot-wire anemometer, is superposition of the uncertainties of the individual acquired voltages converted to velocity. The uncertainty of each individual velocity is determined by non-statistical means based on detailed information of instrumentation, equipment calibration and experiment conditions. The hot-wire anemometer have low drift, low noise and good repeatability and these factors do not add significant uncertainty in comparison with other error sources. A standard pitot-static tube is used to calibrate the hot-wire, for mean velocities more than 5 m/s, the relative standard uncertainty of such system is less than 0.8%. The conversion uncertainty of hot-wire is related to the curve fitting errors. In the present work, the standard deviation of the curve fitting is 0.4%. The uncertainty of the Analog to Digital (A/D) board resolution is determined by $(1/\sqrt{3})(1/U)(E_{\text{AD}}/2^n)(\partial U/\partial E)$, where U is mean velocity, E_{AD} is the A/D board input range, n is its resolution in bits, and $\partial U/\partial E$ is the slope of the calibration curve. In the present work $U = 10$ m/s, $\partial U/\partial E = 3.35$ Volt m/s, $E_{\text{AD}} = 20$ Volt, and $n = 12$ bit. Consequently, the uncertainty in this work is $\pm 0.1\%$. Temperature variations from calibration to experiment or during an experiment introduce errors. In order to reduce these errors, we used a correction factor that causes the temperature errors reduce to 0.1%/°C. For all tests, the variations of air-temperature were more than 4 °C, so the errors are less than $\pm 0.4\%$. Other errors due to ambient pressure variations, humidity,

Fig. 4. Photograph of NLF-0414 airfoil model with ice shape in the test section.

and probe positioning are negligible. Consequently, the total uncertainty of the measurement with hot wire was ±1.7%.

3. Numerical methods

According to complexity of the flow field, incompressible full N-S equations are adopted as governing equations. These equations are discretized using F-V technique. Since the flow velocity is low, the flow field can be considered incompressible. For numerical solution of such flows pressure-based algorithms are appropriate. In these algorithms pressure–velocity coupling is achieved by using a pressure correction equation and iterative procedure. A variety of pressure-based algorithms have been proposed, the efficiency of these algorithms strongly dependent to the flow field that is going to be analyzed. Here we have adopted Pressure Implicit Splitting of Operators (PISO) algorithm which has better convergence rate for the current flow field in comparison with the other algorithms such as SIMPLE or SIMPLER. Generally, for problems in which momentum equations are not coupled to a scalar variable, the PISO algorithm showed robust convergence behavior. PISO algorithm involves one predictor step and two corrector steps. In predictor step discretized momentum equations are solved with a guessed or intermediate pressure field to give velocity components. In the first corrector step pressure and velocity components are corrected and in the second corrector step the discretized momentum equations are solved once again and velocity components and pressure are corrected for the second time. A second-order upwind scheme was used to approximate inviscid fluxes.

The flow field is turbulent and it is necessary to use proper turbulence modeling. The turbulence model that was used for the present study is the two-equation k–ε model (realizable version) this model is proper for flow fields with recalculating regions such as the present flow field. Fig. 5 shows the grid distribution over the iced airfoil. For all cases, the first grid spacing in the normal direction (y1, or minimum wall spacing) was determined according to the boundary layer behavior which leads to $y+$ less than 1.0 for all flow conditions. The study was performed for $Re = 0.5 \times 10^6$ and $Re = 1.8 \times 10^6$. To ensure the independence of the results to computational grid size, several grid distributions were examined and 269801 nodes for iced airfoil is the grid size that leads to grid independent results.

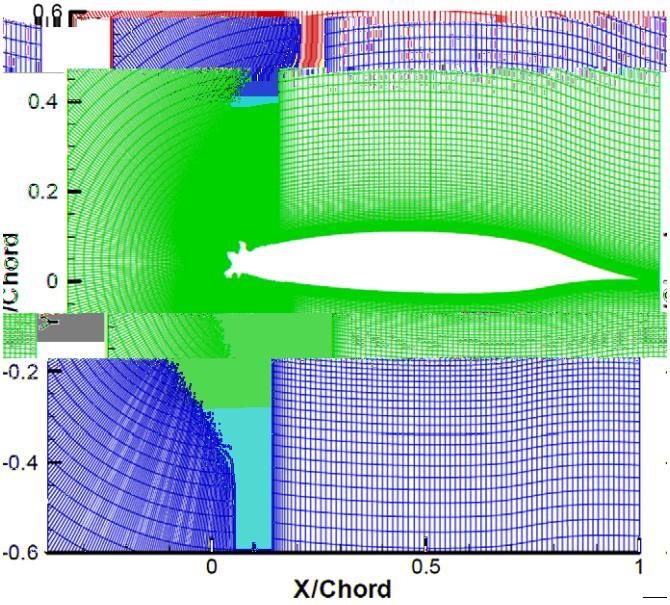

Fig. 5. Iced airfoil grid distribution.

4. Results

In this study Bragg method [9] was employed for estimation of reattachment points for both CFD and experimental simulations. Fig. 6 shows the shear layer reattachment point versus angle-of-attack for glaze-ice from CFD simulation and hot-wires measurements. It can be seen that the numerical results are in good agreement with experimental data except at near to stall. At $\alpha = 6°$, the

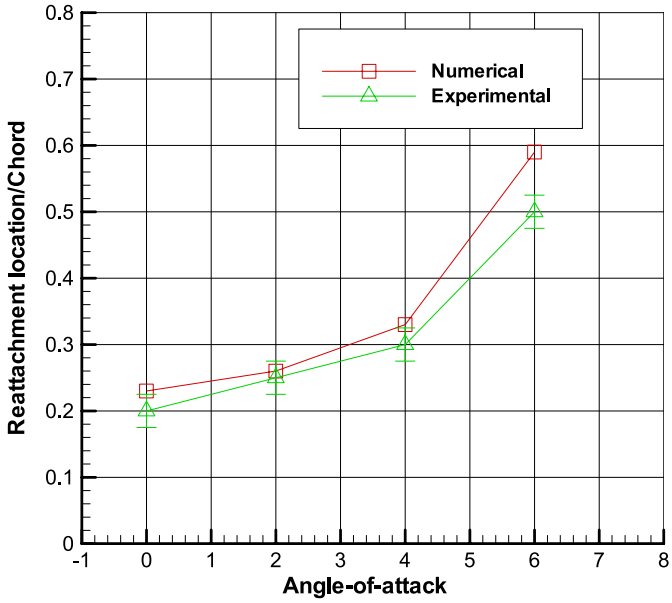

Fig. 6. Comparison of the reattachment location between numerical and experimental.

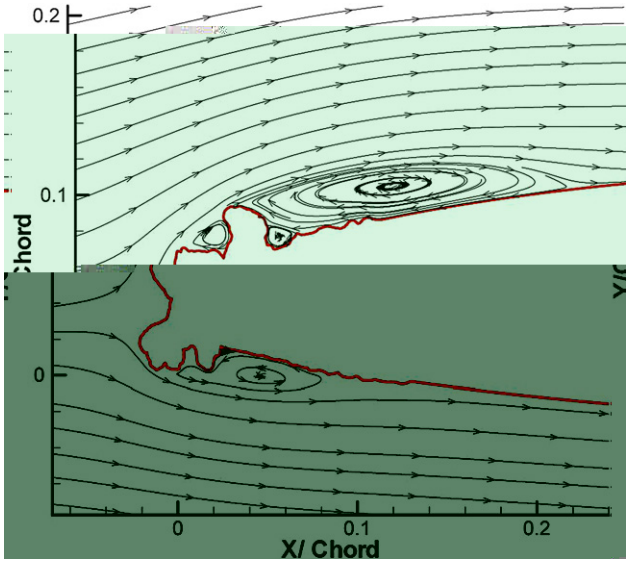

Fig. 7. Streamlines plot for iced airfoil ($Re = 1.8 \times 10^6$, $\alpha = 0$).

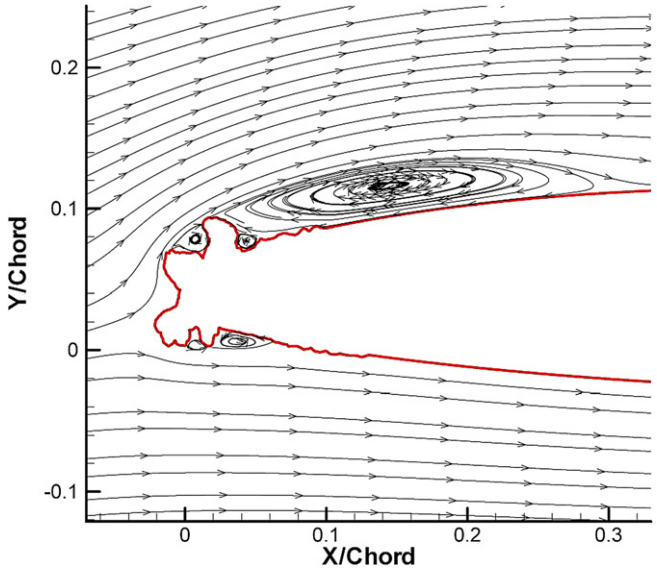

Fig. 8. Streamlines plot for iced airfoil ($Re = 1.8 \times 10^6$, $\alpha = 4$).

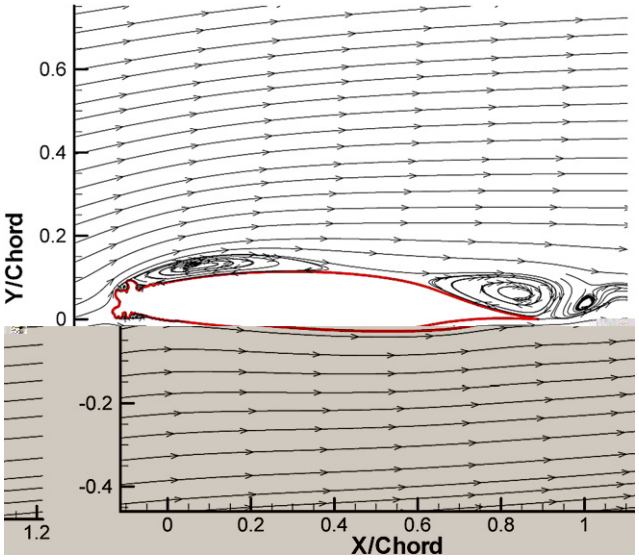

Fig. 9. Streamlines plot for iced airfoil ($Re = 1.8 \times 10^6$, $\alpha = 6$).

numerical results shows a longer bubble and it is due to poor prediction of the flow domain behind the ice accretion at near stall position.

Flow field streamlines predicted by CFD for iced airfoil at $\alpha = 0°, 4°, 6°$ and $8°$ are presented in Figs. 7–10. It can be seen that the separation bubble on the upper surface of the airfoil consisted of two regions: a primary separation bubble region which extended from the tip of the glaze-ice to the reattachment location, with clockwise recirculation and a smaller secondary separated bubble region which forms aft of the ice accretion at the ice–airfoil junction. The main separated bubble length increases with the angle-of-attack but the smaller bubble trapped between the glaze-ice and a little accreted ice behind the main ice and do not change significantly with increasing the angle-of-attack. These phenomenon has been predicted in previous works for NACA0012 [9,10] and for backward-facing step flow investigated by Kostas et al. [13], and Hudy et al. [8]. On the lower surface of the airfoil the same pattern is detected. As the angle-of-attack increases the main separated bubble becomes smaller. The height of the separated bubble is approximately equal to the ice height and has a concave shape which follows the curvature of the airfoil. With increasing the angle-of-attack to $\alpha = 6°$ a separation bubble forms at the trailing edge of the airfoil. At higher angle-of-attack, this separated bubble joints rapidly with the primary separated bubble that has formed aft of the ice accretion and creates a larger bubble with clockwise recirculation on the upper surface ranging from the tip of the ice accretion to trailing edge. This phenomenon leads to the airfoil stall.

Figs. 11–15 depict other results of CFD calculations for the iced airfoil. Fig. 11 shows normalized streamwise velocity contours at $\alpha = 0°$. In this figure a shear layer which forms between separated bubble and high speed inviscid region above the bubble can be detected clearly.

Turbulence intensity contours at angles-of-attack of $\alpha = 0°$, $4°$, $6°$ and $8°$ are presented in Figs. 12–15. A region with large velocity fluctuations is visible in the shear layer. This region is thin near the tip of the ice and then expands to the height of the accreted ice at upstream of the reattachment location. This region extended

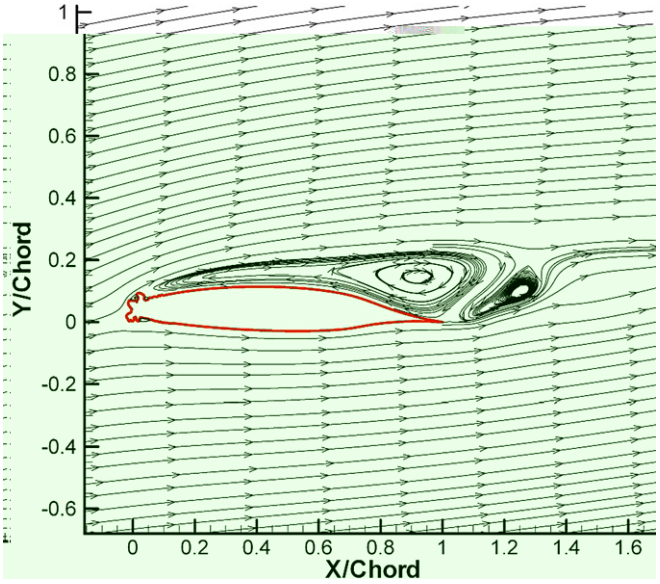

Fig. 10. Streamlines plot for iced airfoil ($Re = 1.8 \times 10^6$, $\alpha = 8$).

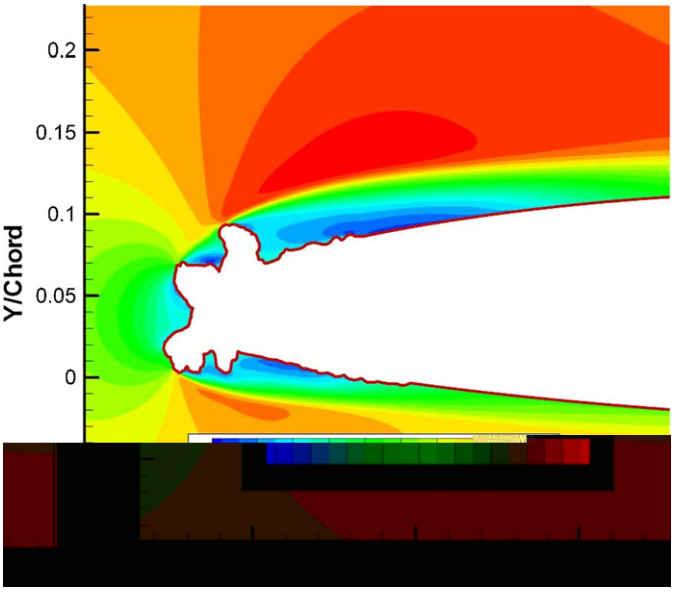

Fig. 11. Normalized streamwise velocity contours for iced airfoil ($Re = 1.8 \times 10^6$, $\alpha = 0$).

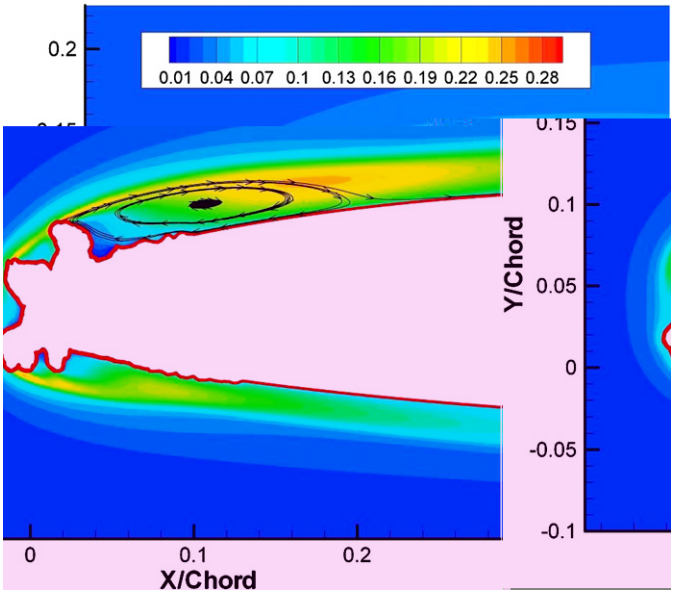

Fig. 12. Turbulence intensity contours for iced airfoil ($Re = 1.8 \times 10^6$, $\alpha = 0$).

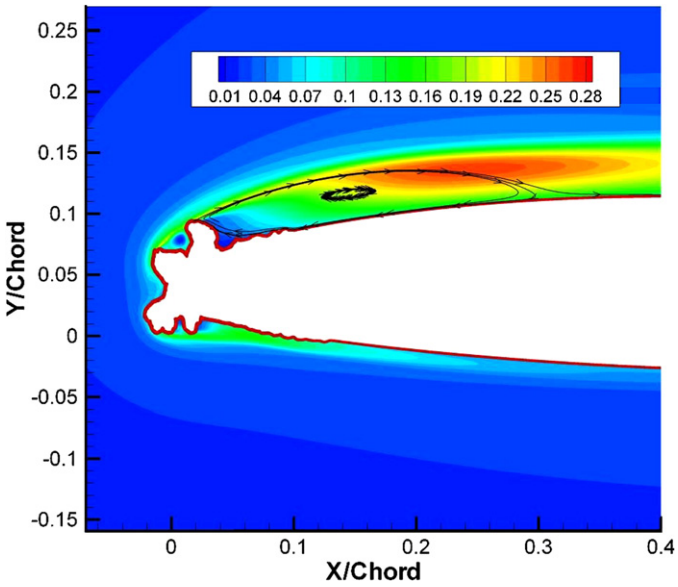

Fig. 13. Turbulence intensity contours for iced airfoil ($Re = 1.8 \times 10^6$, $\alpha = 4$).

to downstream and finally decayed. The region is split up by the separated bubble border. At $\alpha = 0°$ (Fig. 12) the turbulence intensity contours have two local maximum in the shear layer region. The first one is nearly 27.7% and located just downstream of the tip of the ice and the other one is 24.6% and located at the upstream of the reattachment location. The same characteristics of turbulence intensity can be seen in Fig. 13 for $\alpha = 4°$. In fact, the flow pattern did not significantly affected by increasing the angle-of-attack up to $\alpha = 8°$ where the airflow reached to stall conditions. with increasing the angle-of-attack to $\alpha = 8°$, the flow field pattern completely changes as shown in Fig. 15. Such characteristics are reported for NACA 0012 airfoil by Jacobs and Bragg using PIV [10] and Khodadoust [11] using LDV. Similar behavior was also reported by Kostas et al. [13] and Hudy et al. [8] for backward-facing step flow. In an attempt to measure time dependent surface pressure for NACA 0012 by Gurbacki and Bragg [7], a maximum of RMS surface pressure has been detected at upstream of the reattachment point which confirms the above mentioned distribution of the turbulence intensity.

Fig. 16 shows variation of maximum turbulence intensity versus angle-of-attack. In this figure the results of CFD calculations are compared with experimental data. The results of CFD calculations are in good agreement with experimental data. The results of the CFD calculations are over predicted, this can be due to the effects of the turbulence modeling in these calculations. In fact when a turbulence model is employed in a CFD code the model operates on entire points of the flow field but in the wind tunnel experiments, the free stream is nearly laminar (turbulence intensity less than 0.1%). It can be seen that the maximum turbulence intensity upstream of the reattachment location increases with angle-of-attack and then decreases at near stall angles-of-attack.

Fig. 17 shows chordwise distribution of maximum streamwise turbulence intensity of the experimental data at angle-of-attack of $\alpha = 0°$. The data are in good agreement with the numerical results that discussed previously. In this figure the distribution has two maximum points as discussed in numerical results. The decay of

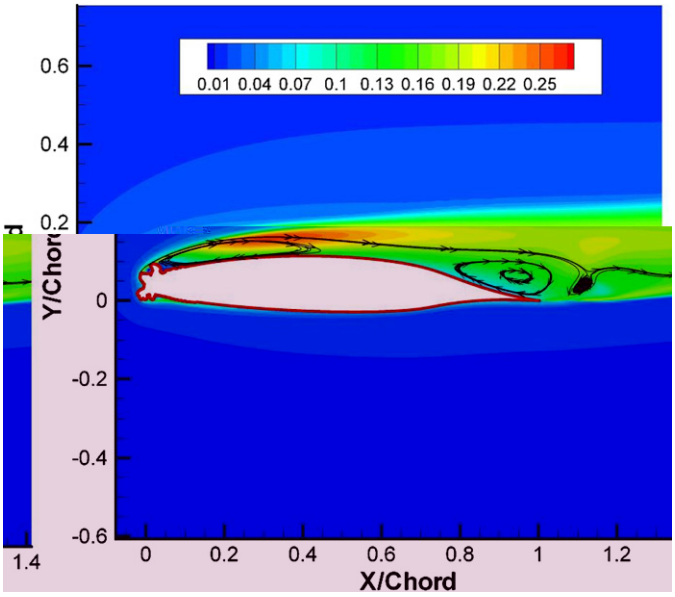

Fig. 14. Turbulence intensity contours for iced airfoil ($Re = 1.8 \times 10^6$, $\alpha = 6$).

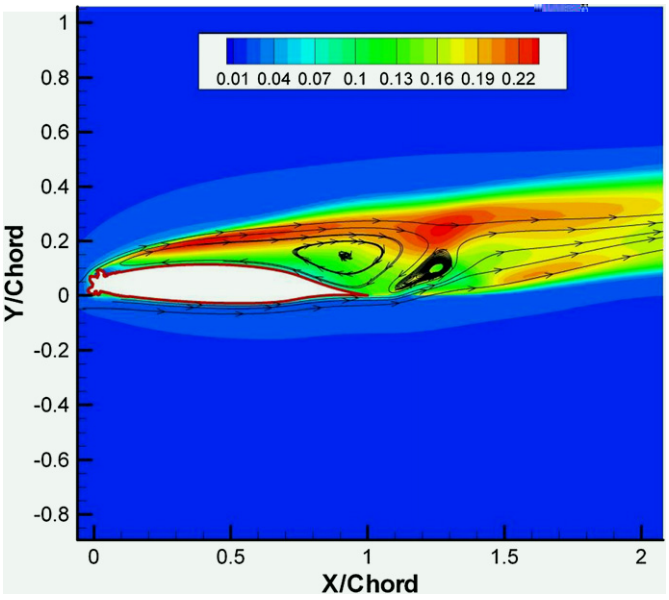

Fig. 15. Turbulence intensity contours for iced airfoil ($Re = 1.8 \times 10^6$, $\alpha = 8$).

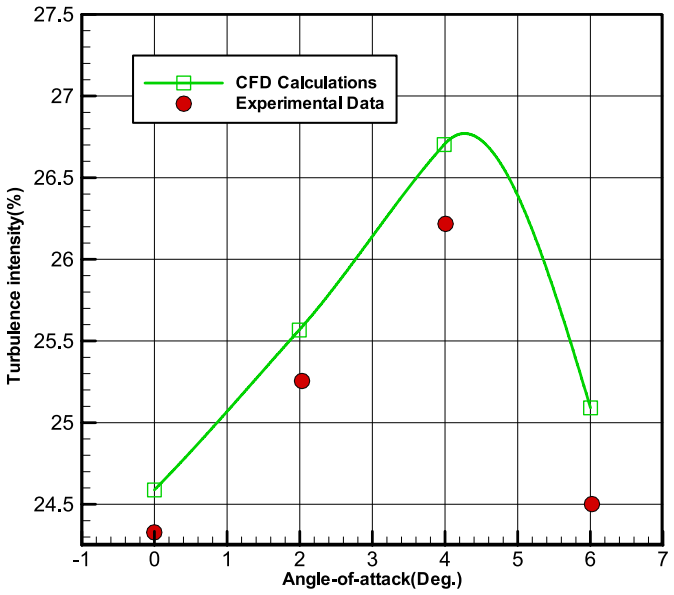

Fig. 16. Maximum turbulence intensity upstream of the reattachment point.

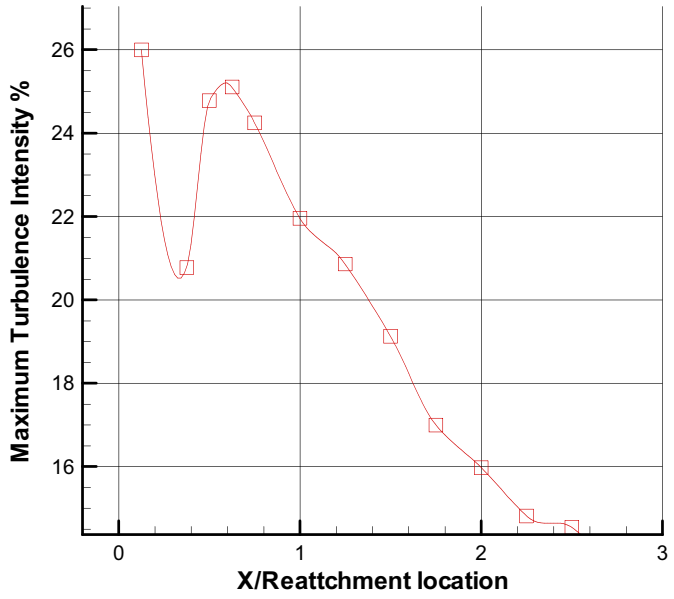

Fig. 17. Chordwise distribution of maximum streamwise turbulence intensity ($Re = 0.5 \times 10^6$, $\alpha = 0$).

the maximum turbulence intensity can also be seen which was predicted by CFD.

As mentioned before the flow field unsteadiness on NACA 0012 airfoil with simulated glaze-ice accretion was reported in [6,7,10]. These unsteadiness on the iced airfoil is due to vortices that form in the shear layer and vortex shedding downstream of the reattachment location in regular frequencies and shear layer vertical flapping in low frequencies.

According to the general trends of the upper-surface velocity spectra, the iced-airfoil flow field unsteadiness associated with the vortices frequency was examined in the velocity spectra at the nearest point to the reattachment location in chord wise. At this point the turbulence intensity is maximum. Fig. 18 shows the experimental regular frequency of the vortices motion in the shear layer of the iced-airfoil at Reynolds number of 0.5×10^6 and angles-of-attack of $\alpha = 0°, 2°, 4°$ and $6°$. The central frequency of the local maximum spectrum amplitude is corresponding to the regular frequency of the vortices. The bandwidth of the local maximum amplitude indicated that the vortex motion in the shear-layer of iced airfoil was not a periodic phenomenon. At $\alpha = 0°$, the local maximum amplitude occurred at frequency of approximately 184 Hz, An increase in angle-of-attack to 2° and 4° revealed a local maximum amplitude at 127 Hz and 59 Hz respectively, and at $\alpha = 6°$, the regular frequency occurred at 52 Hz. It can be seen that the bandwidth of the local maximum amplitude and the frequency of the vortices decrease with increasing the angle-of-attack.

In Fig. 19 non-dimensional frequency or Strouhal number at various angels-of attack are compared qualitatively with Gurbacki and Bragg results for NACA 0012 [6]. The Strouhal number $St = fL_R/V_\infty$ is calculated for each case based on the length of the separation bubble (L_R) and the free stream velocity. Here f is the frequency, L_R is the reattachment location or bubble length, and V_∞ is the free stream velocity. These non-dimensional values, ranging from 0.44 to 0.78 are in good agreement with those of other

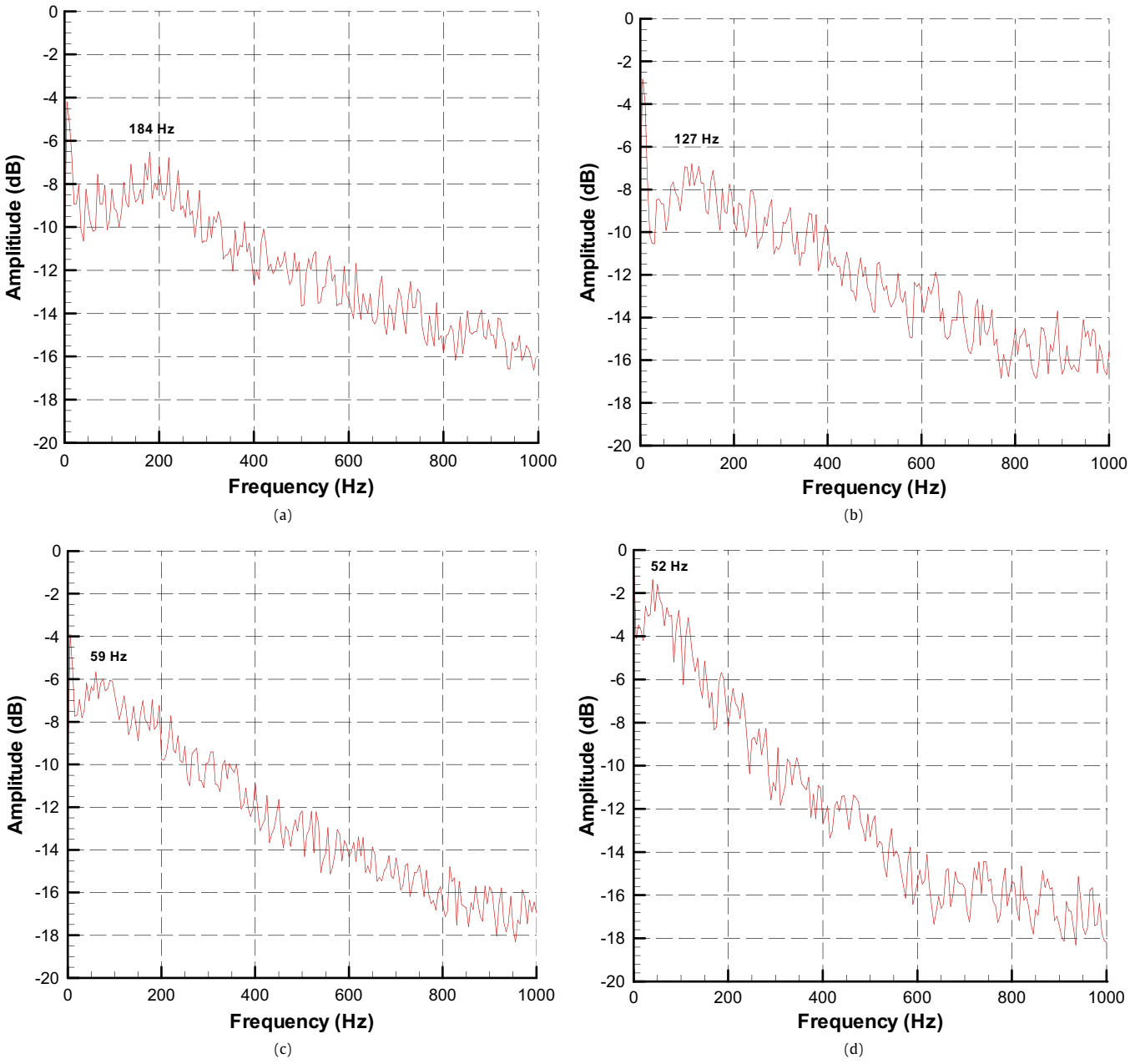

Fig. 18. Vortex frequency, power spectral density function of the time dependent velocity fluctuation near reattachment location ($Re = 0.5 \times 10^6$). (a) ($\alpha = 0$), (b) ($\alpha = 2$), (c) ($\alpha = 4$), (d) ($\alpha = 6$).

separated flow fields reported in [3–6,12]. Gurbacki and Bragg [6] reported the flow field unsteadiness Strouhal numbers of $St = 0.53–0.73$ on NACA 0012 airfoil with two and three-dimensional, simulated, leading edge, glaze-ice accretions. Driver et al. [4] observed the maximum energy in the instantaneous pressure near reattachment at shear layer of the backward-facing step at Strouhal number of 0.6. For the same geometry, Eaton and Johnston [5] reported a value of 0.52 from the power spectrum of the streamwise velocity fluctuations near reattachment. Cherry et al. [3] observed shedding at a non-dimensional frequency of 0.7 from shear-layer velocity fluctuations and finally, Kiya and Sasaki [12] reported values of 0.6 and 0.65 for the vortex shedding on a blunt flat plate.

Fig. 20 shows the frequency of the vortices downstream of the reattachment location at $\alpha = 6°$. These frequencies were captured normal to the chordwise direction where the turbulence intensity is maximum. These data are in good agreement with the results of Driver et al. [4] who reported decreasing in the low frequency content of the surface pressure spectrum downstream of the reattachment location on a backward-facing step. Similar results were observed at other angles-of-attacks. The second unsteady mode identified by Gurbacki [6,7] was associated with very low-frequency oscillations of the separation bubble. These low frequencies could be easily identified in the time-dependent lift or moment coefficients. A sample of instantaneous lift coefficient for NLF-0414 airfoil with simulated glaze-ice accretion at $Re = 1.8 \times 10^6$ and angle-of-attack $\alpha = 7°$ presented in Fig. 21. The frequency of lift oscillation at the presented configuration is approximately 2.5 Hz which is equivalent to Strouhal number of 0.012. The important consequence of this phenomenon is that very-large force fluctuations occurred at very low frequency. Particularly, this can have an effect on structural airframe/component vibrations and response. The non-dimensional frequency clearly is in good agreement with previous studies on NACA 0012 with simulated leading edge glaze-ice accretion [7,14].

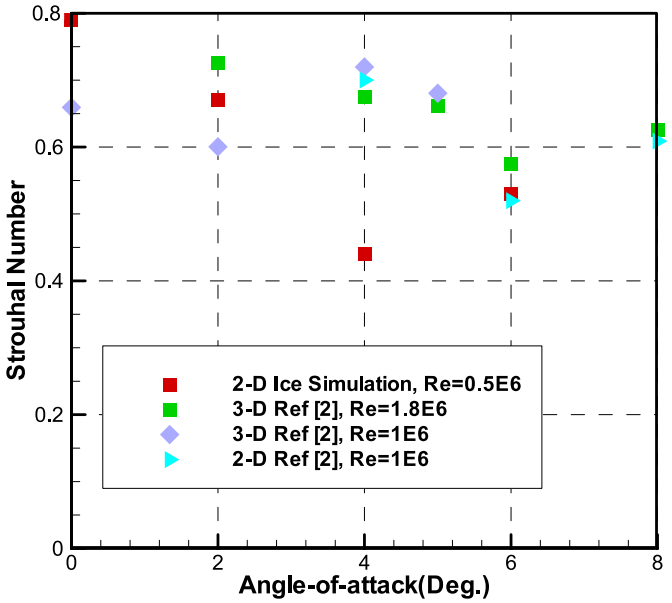

Fig. 19. Comparison of variation the Strouhal number with angle-of-attack with Ref. [2].

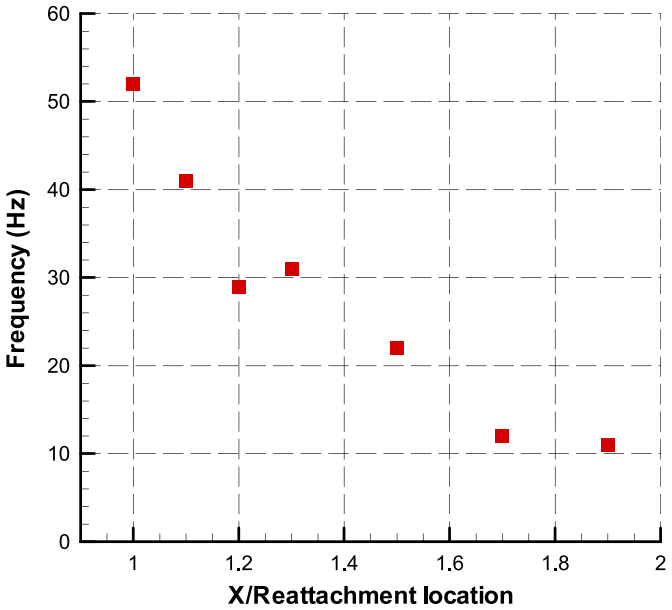

Fig. 20. Vortex frequency distribution downstream of the reattachment location ($Re = 0.5 \times 10^6$, $\alpha = 6$).

5. Conclusions

The main goal of this investigation was to understand the flow field structure of the separation bubble formed on NLF-0414 airfoil with glaze-ice accretions using CFD and hot-wire anemometry and comparing these results with previous researches performed on NACA 0012 airfoil.

In general, the CFD results show that the flow field with two-dimensional ice simulations consisted of a main primary clockwise recirculating separation region enclosed by a shear layer and a small, counterclockwise recirculating, and secondary separation region formed behind the intersection of the ice and airfoil. It was found that the primary separation bubble grew with increasing angle-of-attack. The shear layer formed between the primary separation bubble and the high velocity inviscid flow above the airfoil and consist of two high turbulence intensity region, The first re-

[9] Jason J. Jacobs, Michael B. Bragg, Particle image velocimetry measurements of the separation bubble on an iced airfoil, in: 24th AIAA Applied Aerodynamics Conference, San Francisco, CA, 5–8 June 2006.

[10] Jason J. Jacobs, Michael B. Bragg, Two- and three-dimensional iced airfoil separation bubble measurements by particle image velocimetry, in: 45th AIAA Aerospace Sciences Meeting & Exhibit, Reno, NV, January 8–11, 2007.

[11] A. Khodadoust, An experimental study of the flowfield on a semispan rectangular wing with simulated glaze ice accretion, Ph.D. thesis, University of Illinois at Urbana-Champaign, Urbana, IL, 1993.

[12] M. Kiya, K. Sasaki, Structure of a turbulent separation bubble, Journal of Fluid Mechanics 137 (1983) 83–113.

[13] J. Kostas, J. Soria, M.S. Chong, Particle image velocimetry measurements of a backward-facing step flow, Experiments in Fluids 33 (2002) 838–853.

[14] K.B.M.Q. Zaman, M.G. Potapczuk, The low-frequency oscillation in the flow over a NACA 0012 airfoil with an iced leading edge, in: T.J. Mueller (Ed.), Low Reynolds Number Aerodynamics, Springer-Verlag, New York, 1989, pp. 271–282.